RSC Advances

PAPER

View Article Online
View Journal | View Issue

Cite this: *RSC Adv.*, 2025, **15**, 47666

High-efficiency RhB dye degradation using β-FeOOH nanorods *via* tribocatalysis

Muhammad Qasim,*[a] Arslan A. Rizvi,[b] Haroon Rashid,[a] Xianglin Li,[a] Hassan A. H. Alzahrani,[c] Raed H. Althomali,[d] Majed M. Alghamdi,[e] Adel A. El-Zahhar,[e] Gideon F. B. Solre*[f] and Sana Ullah Asif*[a]

Tribocatalysis respresents a transformative approach with significant implications for electrochemical innovations, sustainable energy technologies, and the efficient remediation of water contaminants. The practical implementation of such systems requries catalysts that combine superior performance with economic and enviromental viability. In this study, we investigate the tribocatalytic activity of β-FeOOH nanorods, systematically examining the effects of key morphological features, including diameter, surface area, and surface roughness. Our results reveal that the nanorods diameter critically influences catalytic performance, with the optimized (β-FeOOH-100 °C) catalyst exhibiting outstanding activity under ultrasonic vibration. This catalyst enables rapid degradation of rhodamine B (RhB) achieving complete mineralization within 30 minutes, a high rate constant of 0.19 min^{-1}, and excellent stability. Mechanistic studies indicate that friction-generated H^+ ions facilitate the formation of reactive $^{\bullet}OH$ and $^{\bullet}O_2^-$ radicals, which drive efficient pollutant decomposition. Overall, this work elucidates the structure–activity relationship in tribocatalytic materials and positions β-FeOOH nanorods as a promising platform for leveraging mechanical energy in the treatment of organic-contaminated wastewater.

Received 10th September 2025
Accepted 14th November 2025

DOI: 10.1039/d5ra06827d

rsc.li/rsc-advances

Introduction

Water is integral to sustainability as it plays a crucial role in safeguarding ecosystems and facilitating socio-economic development.[1–3] Consequently, there is an imperative need for highly efficient wastewater treatment technologies to manage the purification of industrial effluents and alleviate environmental damage.[4,5] Wastewater typically contains intricate organic pollutants and heavy metals, rendering the treatment process exceedingly complex and protracted.[6–8] The assurance of reliable and safe access to sources of clean water represents a formidable challenge in the contemporary epoch. Poorly managed treatment of detrimental organic pollutants, including organic dyes, biphenyls, medicines, chemical pesticides, phenols, agricultural products, carbohydrates, polymer adititives, and surfactants, poses a threat to human health and upsets the natural equilibrium of ecosystems.[9–12] The swift progression in developing novel methods for dye wastewater treatment is of paramount importance. Multiple traditional techniques, such as membrane filtration, biological processes, physical adsorption, chemical precipitation, electrochemical oxidation, and coagulation have proven efficacious in eliminating organic contaminants from water during the wastewater treatment process.[13–15] Nevertheless, it is critical to recognize that these procedures may inadvertently lead to secondary contamination.

Tribocatalysis constitutes an innovative sustainable technology that leverages the catalytic properties of particular materials in conjunction with mechanical energy to facilitate environmental remediation.[16] This process entails the formation of active charge carriers and highly reactive surface sites on catalysts *via* frictional forces, thereby initiating a series of oxidation and reduction reactions. Nonetheless, the catalytic efficiency and practical applicability of tribocatalysis, including parameters such as energy conversion efficiency and scalability, continue to present significant limitations.[17] Similarly, photocatalysis represents a sustainable technology that exploits the catalytic characteristics of semiconductors in tandem with solar illumination to effectuate environmental remediation.[18–20] This process involves the excitation of e^-/h^+ pairs within semiconductors when exposed to light, initiating a sequence of oxidation and reduction reactions on the surface of

[a]*Department of Physics, Qilu Institute of Technology, Jinan 250200, Shandong, P.R. China. E-mail: qasim@qlit.edu.cn; sanaullahasif@gmail.com*

[b]*Department of Computer Science and Informatics, Berlin School of Business and Innovation, 12043, Karl-Marx Straße, Berlin, Germany*

[c]*Department of Chemistry, College of Science, University of Jeddah, P. O. Box 355, Jeddah, Saudi Arabia*

[d]*Department of Chemistry, College of Science and Humanities in Al-Kharj, Prince Sattam Bin Abdulaziz University, 11942 Al-Kharj, Saudi Arabia*

[e]*Department of Chemistry, College of Science, King Khalid University, P. O. Box 9004, Abha 61413, Saudi Arabia*

[f]*Department of Chemistry, Thomas J. R. Faulkner College of Science, Technology, Environment and Climate Change, University of Liberia, 00231 Monrovia, Montserrado County, Liberia. E-mail: gideonfbsolre@gmail.com*

semiconductor.[21] However, the catalytic efficacy and pragmatic usability of photocatalysis such as a restricted wavelength range and suboptimal solar energy utilization are the major constraints. In addition, several alternative methodologies, including piezocatalysis, thermocatalysis, pyrocatalysis, and their combinations, have been explored.[22–24] Piezocatalysis notably requires piezocatalysts with non-centrosymmetric crystalline structures that are easily deformable. When a piezo-catalyst is distorted, it generates a piezoelectric field that advances the piezocatalytic process. As a result, the field of piezocatalysis faces a significant challenge due to the limited availability of suitable materials.[25] Tribocatalysis emerges as a pioneering and advanced methodology developed for the purification of colored effluent.[26] The tribocatalysis process is critically dependent on friction, which, through the generation of triboelectric energy, facilitates the augmented breakdown of organic contaminants and dyes. The scientific community has currently delineated two operative mechanisms to explain this phenomenon: the excitation of electrons and the subsequent transfer of electrons between atoms.[16]

The limitations of conventional catalytic processes by harnessing the minimal mechanical energy present in environment to degrade wastewater. Tribocatalysis is characterized by the synergistic interplay between mechanical friction and ensuing chemical reactions on the catalyst's surface.[27] Notably, this process does not require specific physical characteristics, allowing for the utilization of tribocatalysts with a centrosymmetric crystal lattice. This property expands the range of applicable materials. Additionally, tribocatalysis capitalizes on the plentiful and renewable mechanical energy in the environment, thereby reducing energy consumption and mitigating environmental issues.[27] Nevertheless, it is imperative to investigate tribocatalytic materials that are environmentally benign, cost-effective, and highly efficient for practical applications. In a standard tribocatalytic system, the mechanical contact and relative motion of two distinct materials under external force give rise to surface charges of opposite polarity, which then engage with oxygen molecules to produce reactive oxygen species.[27]

Recent developments in tribocatalysis have expanded its utility across multiple domains, including renewable energy production *via* water splitting, formation of combustible gases, organic pollutant degradation, and novel methodologies for environmental cleanup.[28,29] These findings suggest that tribocatalysis possesses considerable potential for a broad spectrum of applications through the utilization of mechanical energy, particularly in the context of wastewater treatment. However, its practical implementation is limited by low catalytic efficiency and optimization.

In the domain of wastewater treatment, substantial advantages exist in the treatment and reuse of wastewater particularly originating from industrial sources to render it suitable for irrigation purposes.[30] Tribocatalytic-based nanomaterials are essential for achieving this goal due to their highly reactive active sites. The principal disadvantages include the facile conversion into secondary pollutants, the utilization of powder catalysts that are challenging to retrieve, and the presence of diverse pollutants that restrict their feasibility for industrial-scale applications. Consequently, the effective implementation of tribocatalytic technologies is contingent upon tribocatalysts that are environmentally sustainable, cost-effective, and exhibit excellent performance.[27]

β-FeOOH also referred to as akaganeite, is a semiconductor comprised of the earth-abundant element iron (Fe).[31] Consequently, it demonstrates significant potential as a catalyst owing to its abundant availability, low cost, environmentally benign characteristics, and relatively high stability. Conventionally, β-FeOOH is extensively utilized within the domain of photo-electro catalysis; nonetheless, its tribocatalytic efficiency remains uncertain. We have synthesized β-FeOOH nanorods through a straightforward hydrothermal process at various reaction temperatures, allowing for precise control over their size and surface texture. The optimized β-FeOOH nanorods exhibited remarkable tribocatalytic properties in relation to the degradation of rhodamine B (RhB) dye. Initially, the average diameter of the nanorods increased, reaching a peak for the optimized catalyst before decreasing, while the surface area initially decreased and subsequently increased with rising temperatures. These observations are well-aligned with the tribocatalytic performance of the nanorods. The optimized catalyst effectively degrades RhB dye under the influence of ultrasonic vibrations. The significance of this research lies in the environmentally friendly synthesis at low temperatures and its potential as a promising catalyst for wastewater treatment through the application of vibrational mechanical energy.

Results and discussion

The complete synthesis method is described in SI and synthesis route of the catalyst is shown in Scheme 1. Next, the phase and functional group identification analysis were performed. Fig. 1a depicts the X-ray diffraction (XRD) patterns of β-FeOOH nanorods synthesized at varying reaction temperatures from 80 to 120 °C to ascertain the mineral phase and purity. The diffraction peaks observed correspond closely with the standard diffraction data (JCPDS no: 34-1266), space group: *Pbnm*, indicating that all three samples are composed of pure-phase orthorhombic crystals with a centrosymmetric structure.[31] The diffraction peaks broaden as the synthesis temperature increases, indicating smaller crystallite size. The crystallite size of the β-FeOOH nanorods were calculated using the Scherrer equation, and found to be correlated with the synthesis temperature as shown in Fig. S2.

Moreover, no peaks indicative of impurities such as α-FeOOH, γ-FeOOH, and α-Fe_2O_3 were detected. The presence of prominent and well-defined diffraction peaks further suggests that the synthesized materials possess excellent crystallization.

To examine the chemical structure and the functional groups responsible for RhB dye degradation, Fourier Transform Infrared (FTIR) analysis is conducted. Fig. 1b illustrates the FTIR spectrum of the β-FeOOH nanorods prepared employing the hydrothermal route. Previous studies underscore the necessity of evaluating characteristic peaks to analyze and validate the accurate chemical synthesis of β-FeOOH nanorods.

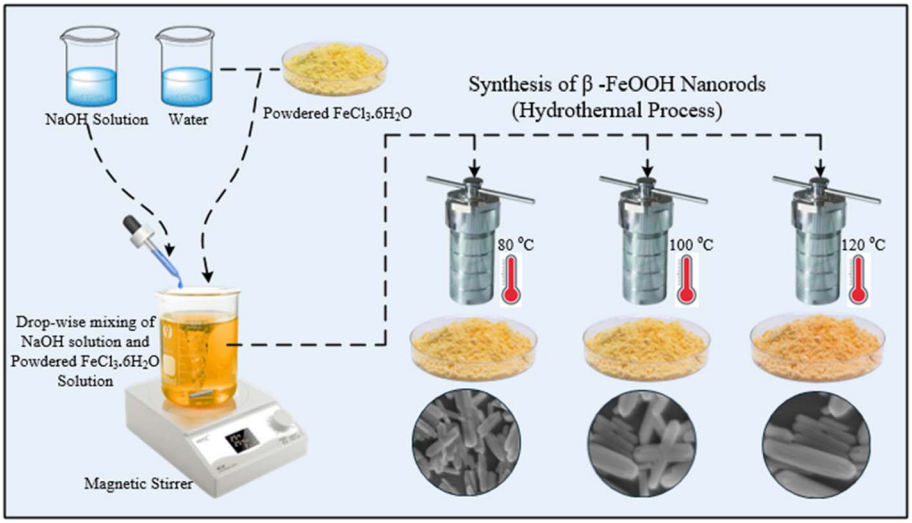

Scheme 1 Complete synthesis route of β-FeOOH nanorods at different temperatures *i.e.*, 80 °C, 100 °C, and 120 °C, respectively.

The β-FeOOH nanorods exhibit FeO_6 octahedral units, characterized by distinct peaks corresponding to two significant vibrational bands of Fe–O and OH groups. The absorption peaks that arise between 450 and 800 cm^{-1} are frequently attributed to basic vibrating groups of inorganic ions. The bending vibration, symmetric stretching, and asymmetric stretching vibrations of Fe–O octahedral groups were observed at 470 cm^{-1}, 500 to 530 cm^{-1}, and 642 to 795 cm^{-1}, respectively. Furthermore, the structural band (Fe–OH) emerges at the bending vibration of 890 cm^{-1}, confirming the presence of structural groups (OH) within the octahedra of β-FeOOH nanorods. The spectral band around 1030 cm^{-1} is ascribed to the diminished hydrogen bonds between water molecules and bridging hydroxyl groups of the β-FeOOH structure. Meanwhile, the band that arises at 1155 cm^{-1} corresponds to the δ(OH) vibrational modes of the bridging hydroxyl group [Fe–O(H)–Fe].

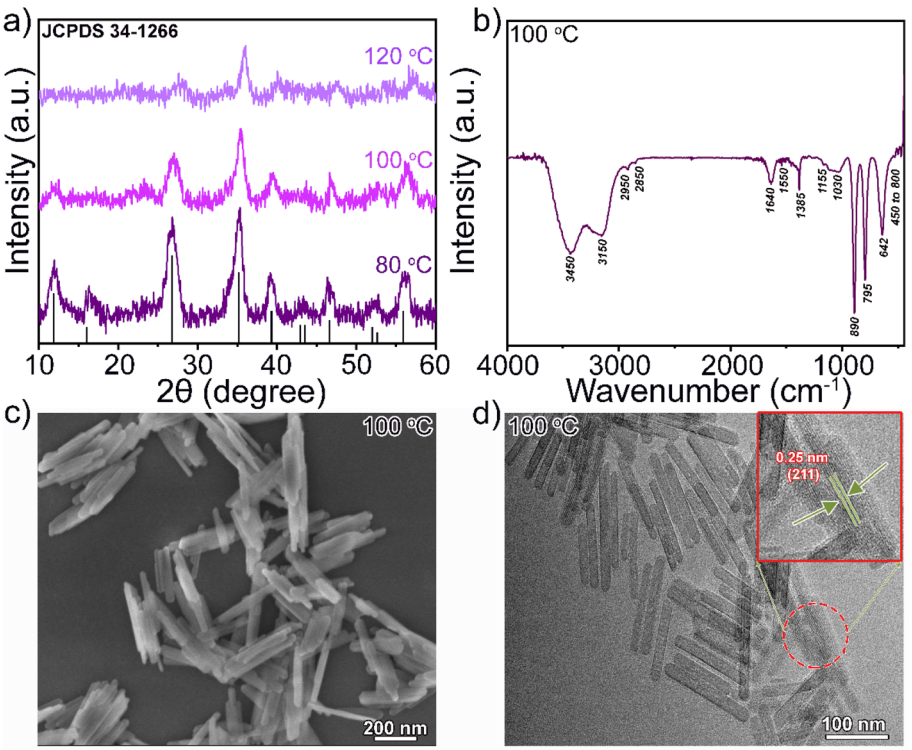

Fig. 1 (a) X-ray diffraction (XRD) spectra taken from the β-FeOOH nanorods synthesized at various reaction temperatures. (b) FTIR spectra analysis (c) Scanning Electron Microscopy (SEM), and (d) Transmission Electron Microscopy analysis of β-FeOOH nanorods. The inset in (d) displays HRTEM analysis of the nanorods.

Similarly, the vibrational band observed at 1385 cm^{-1} which is attributed to the asymmetric stretching mode of carbonate ions (CO_3^{2-}). This is a common feature in materials synthesized in basic aqueous environments and originates from the reaction of sodium hydroxide with atmospheric carbon dioxide during the preparation process. Peaks occurring at 2850 and 2950 cm^{-1} are attributed to the presence of organic pollutants. However, consistent with the previous analysis, the stretching and bending vibration modes rise in the region of approximately 3150, 3428 cm^{-1} and 1550, 1640 cm^{-1}, respectively, indicating the presence of potentially adsorbed water molecules in β-FeOOH nanorods. Our results demonstrate that the structural Fe–O framework and surface hydroxyl groups interact together to degrade RhB dye tribocatalytically, indicating their potential for environmental remediation. To verify the morphology of the catalyst, scanning electron microscopy (SEM) analysis was subsequently performed. Fig. 1c shows the SEM image of the optimized β-FeOOH (*i.e.*, 100 °C) catalysts, illustrating the consistent nanorod structure of the catalyst. SEM analysis confirmed that other samples of β-FeOOH synthesized at different temperatures (*i.e.*, 80, 120 °C) also formed nanorods. The β-FeOOH-120 and β-FeOOH-100 nanorods had furrowed patterns on their surfaces, whereas the surfaces of the FeOOH-80 nanorods were smoother (as shown in Fig. S1). Fig. 1d displays the transmission electron microscopy (TEM) and high-resolution transmission electron microscopy (HRTEM) investigation of the optimized catalyst β-FeOOH-100. The findings align with the SEM analysis, demonstrating that β-FeOOH exhibits a rod-like morphology with an average diameter spanning from 15 nm to 45 nm. This observation is further corroborated by the High-Resolution Transmission Electron Microscopy (HRTEM) analysis, as illustrated in the inset of Fig. 1d. The detected lattice spacing of 0.25 nm corresponds to the {211} crystal plane of β-FeOOH. The TEM image elucidated a flawless and highly organized structure, affirming that these nanorods were highly crystalline. TEM investigations disclosed that all other β-FeOOH samples consisted of nanorods. The average diameters of the nanorods progressively increased, peaking for β-FeOOH-100, and subsequently diminished as the reaction temperature was elevated.

Subsequently, the technique of X-ray photoelectron spectroscopy (XPS) was employed to examine the surface elemental compositions and chemical states of the β-FeOOH catalyst as depicted in Fig. S3. X-ray Photoelectron Spectroscopy (XPS) is an efficacious method for probing the surface chemistry of materials, delivering quantitative and chemical state data pertinent to surface elements. The principal focus is to explore the presence of Fe and O, which determine the chemical attributes and reactivity. The high-resolution XPS spectrum of β-FeOOH nanorods exhibited two distinct peaks with binding energies of 711.7 eV and 725.4 eV, corresponding to the Fe $2p_{3/2}$ and Fe $2p_{1/2}$ spin–orbit doublets, respectively, as illustrated in Fig. S3a. These peaks strongly evidence iron in the +3-oxidation state, verifying the presence of Fe(III) in the nanorods. The peak at 711.7 eV clearly indicates the Fe(III) oxidation state, aligning with the values anticipated for iron oxyhydroxides.[2,32,33] Furthermore, a satellite peak was also observed, often linked to Fe(III) species. This satellite peak originates from the shake-up transitions typical of Fe(III), distinguishing it from other iron oxide phases such as Fe_2O_3 or Fe_3O_4. This observation is crucial, as it assists in distinguishing β-FeOOH from other iron oxide variants that may display analogous binding energies yet differ in their electronic structure. The O 1s spectrum of β-FeOOH nanorods is critical for elucidating the various oxygen environments within the material. For β-FeOOH nanorods, three distinct peaks manifest at binding energies of approximately 529.74 eV, 531.31 eV, and 532.73 eV, respectively, as shown in Fig. S3b. The peak arises at 529.74 eV indicates the lattice oxygen (O_2^-) within β-FeOOH nanorod structure, specifically the oxygen atoms directly bound to iron (Fe–O) bonds in the crystal lattice. This characteristic signifies the material's rigidity and stability. Similarly, the peak at 531.31 eV is associated with surface hydroxyl groups (OH^-). This group is vital for surface reactivity and influences the adsorption characteristics of β-FeOOH nanorods, enhancing its applications in catalysis and environmental remediation.[34] Finally, the peak at 532.73 eV indicates the adsorbed water molecules or loosely bound oxygen-containing species. Water molecules can adhere to the surface due to the polar nature of β-FeOOH, which can attract and retain water molecules *via* hydrogen bonding.

The tribocatalytic efficiencies of the β-FeOOH nanorods, synthesized at various reaction temperatures, were initially assessed by evaluating the degradation of RhB under ultrasonic vibration, as illustrated in Fig. 2. Fig. 2a–c illustrates the temporal variation of UV-vis absorption spectrum of RhB solution degraded by β-FeOOH catalysts prepared at different temperatures. The intensity of the principal absorption peak in the UV-visible spectrum decreases progressively with prolonged stirring time. It is inferred from these analyses that the tribocatalytic activity of the optimized catalyst (*i.e.*, β-FeOOH-100 °C) achieves maximum degradation under the same conditions. Lastly, the degradation efficiency curve corresponding to the provided data is presented in Fig. 2d.

The surface area is a critical parameter in the field of catalysis; generally, a larger surface area provides a greater number of active sites, enhanced reaction kinetics, improved mass transfer, and optimized electron–hole dynamics, essential for catalytic reactions.[30] With this consideration, we conducted nitrogen gas adsorption–desorption isotherms on the β-FeOOH catalyst as illustrated in Fig. S4. Following meticulous calculations, the results indicated that the BET surface areas of these samples initially increased, followed by a slight decrease as the reaction temperature rose. Furthermore, tribocatalytic reactions were employed, as these reactions occur on the catalyst's surface. To elucidate the factors contributing to the variable tribocatalytic activity of β-FeOOH nanorods, the interrelationships among the average diameter, surface area, and k values are summarized in Fig. 3a. It is apparent that the surface area of these β-FeOOH nanorods decreased with an increase in reaction temperature, reaching a minimum at 120 °C. The inconsistencies in the correlation between the surface areas of various catalysts and their tribocatalytic performances suggest that the surface area does not significantly impact tribocatalytic performance. Consequently, the average diameters of β-FeOOH

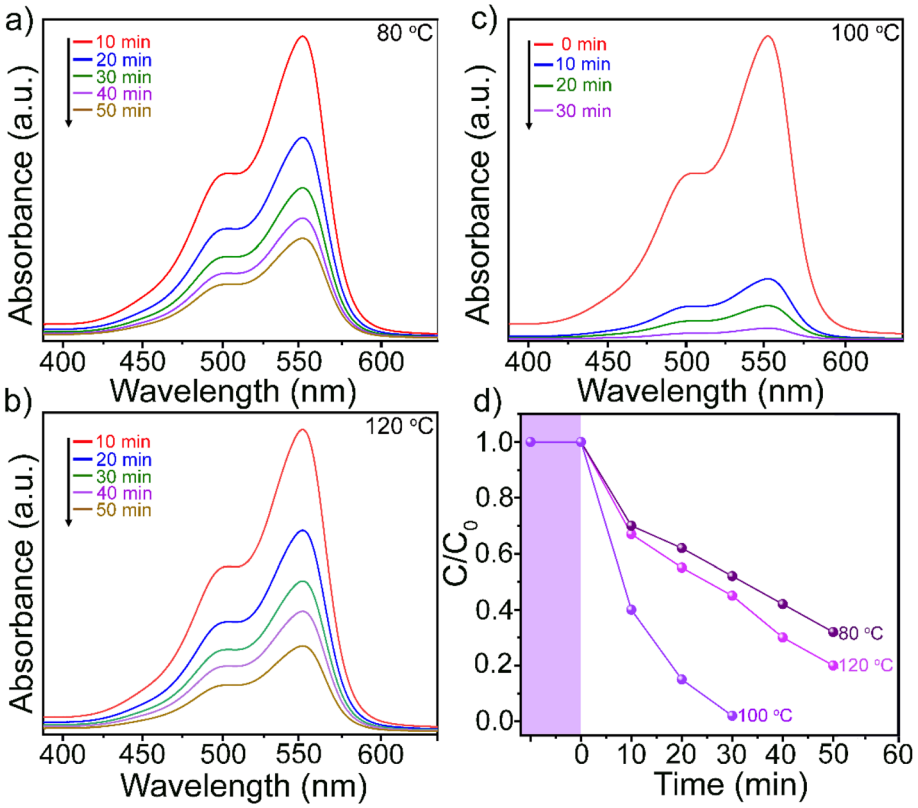

Fig. 2 The absorption spectra of RhB aqueous solution were measured over time using β-FeOOH catalyst produced at three different temperatures: (a) 80 °C, (b) 100 °C, and (c) 120 °C, respectively and (d) the related degrading efficiency curves.

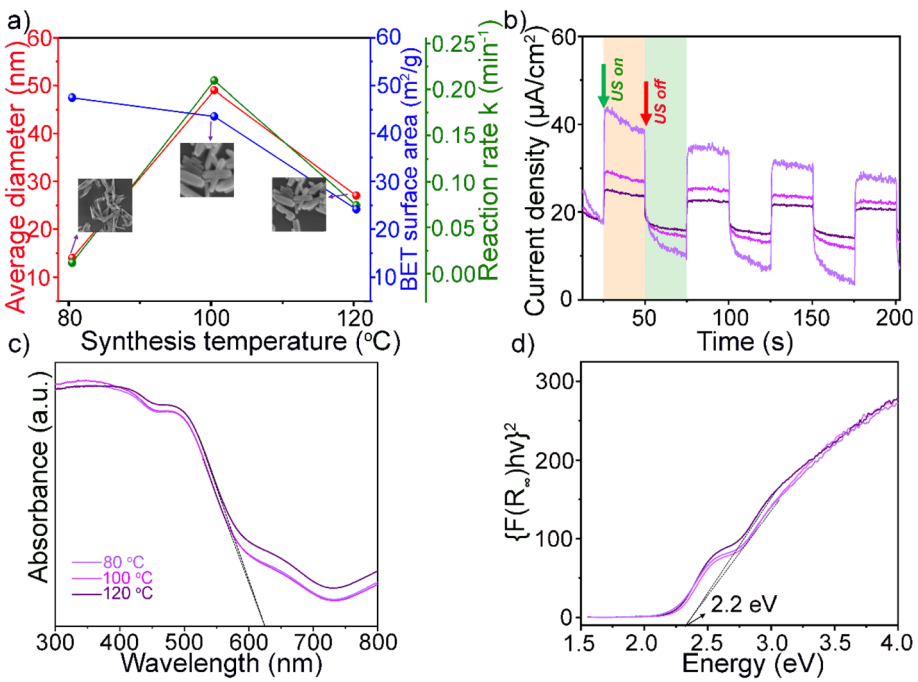

Fig. 3 (a) The mean diameter and surface area of β-FeOOH catalyst synthesized at various temperatures are plotted, with corresponding SEM images shown in the insets. (b) Transient tribocurrent density-time analysis of optimized β-FeOOH catalyst. (c) UV-vis spectra analysis of β-FeOOH catalyst at different temperature, and (d) the corresponding band gap analysis.

nanorods were also examined. The average diameters of the nanorods initially increased, achieving their maximum size at 100 °C before decreasing. A correlation was observed between the average diameters of the nanorods and their tribocatalytic performances, suggesting that the diameters of the nanorods considerably influenced their tribocatalytic performances. The optimized catalyst possesses the largest average diameter and exhibits the highest tribocatalytic performance compared to the other catalysts synthesized at different temperatures. This suggests that the (β-FeOOH-100 °C) catalyst undergoes a more intense reaction with water molecules and generates a greater number of charges than the other catalysts under identical conditions as demonstrated in Fig. 3c. Scanning Electron Microscopy (SEM) analysis was further utilized to investigate the microstructure of these catalysts as shown in the insets of Fig. 3a. The β-FeOOH-80 °C and β-FeOOH-120 °C catalysts possess similar morphologies, yet the former has a larger average diameter than the latter. As previously indicated, the tribocatalytic performance was predominantly influenced by larger diameters rather than surface roughness, leading to enhanced activity. Fig. 3b illustrates the time-dependent analysis of tribocurrent density for the optimized catalyst under ultrasonic vibration. The optimized catalyst exhibited the highest tribocurrent density. These finding suggests that the optimized catalyst (β-FeOOH-100 °C) generated a greater number of charges compared to other nanorods under equivalent conditions, corroborating its superior tribocatalytic performance. In conclusion, the diameter of nanorods exerted a significant influence on tribocatalytic activity, in contrast to other factors such as electrical structure, surface area, and roughness.[30] Subsequently, the electronic structures of β-FeOOH nanorods were analyzed using UV-vis diffuse reflectance spectra, as illustrated in Fig. 3c. The absorption edges for the three catalysts did not demonstrate any discernible differences. The bandgaps (E_g) of these catalysts are depicted in Fig. 3d. The calculated energy bandgap (E_g) values of the β-FeOOH nanorods were determined to be 2.2 eV. This indicates that the catalysts synthesized at different temperatures did not exhibit variations in bandgap. The valence band potential of the β-FeOOH nanorods was determined using XPS-VB analysis, as shown in Fig. S5a. The estimated valence band value relative to the conventional hydrogen electrode (NHE) was computed to be 1.53 eV. Consequently, the conduction band value of the β-FeOOH nanorods was −0.67 eV relative to the normal hydrogen electrode (NHE). Based on these calculations, the energy band diagram is portrayed in Fig. S5b. To verify the conduction band (CB) of synthesized β-FeOOH nanorods, with respect to reference electrode (Ag/AgCl) at a pH of 7 Mott–Schottky (MS) analysis was employed as shown in Fig. S6. The flat-band potential (E_{fb}) was determined to be −0.89 V. Using the slop derived from MS plots and using eqn (1) and (2) as provided in SI the CB potential is −0.67 eV. The energy levels derived from this electrochemical analysis are in strong agreement with our XPS valence band spectrum and provide a robust and experimentally verified foundation for the proposed energy band diagram and the subsequent discussion on the charge transfer mechanism in the tribocatalytic process.

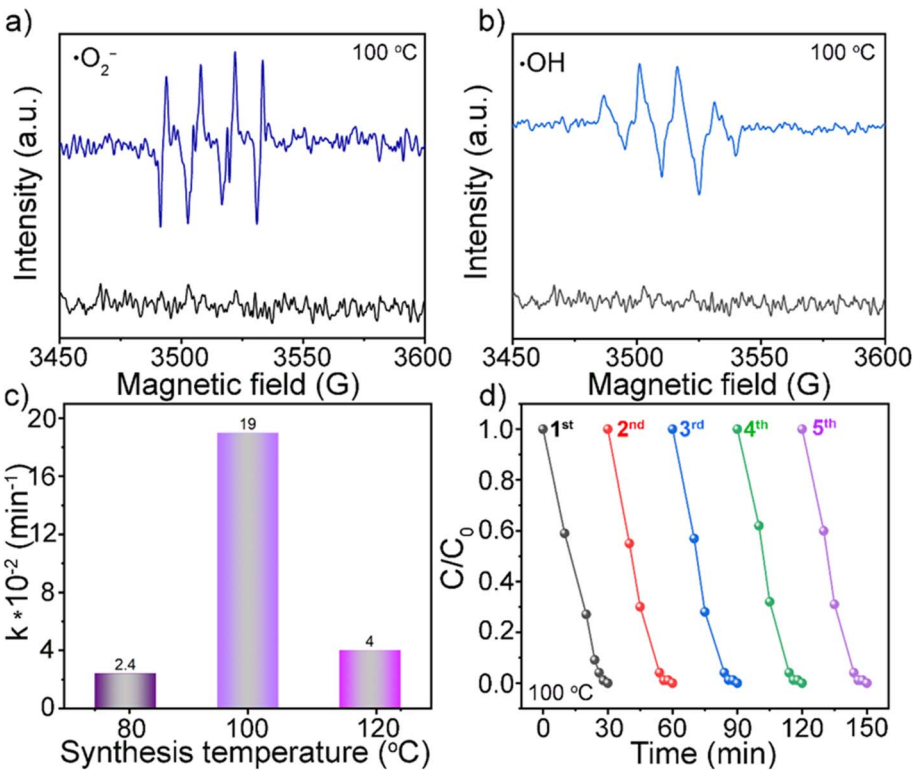

Fig. 4 (a and b) EPR spectrum analysis for detection of $^{\bullet}O_2^-$ detection, and $^{\bullet}OH$ respectively. (c and d) comparison analysis of the reaction rate constant of β-FeOOH synthesized at different temperatures, and stability analysis for the degradation of RhB, respectively.

Next to verify the generation of $^{\bullet}OH$ and $^{\bullet}O_2^-$ active radicals, electron paramagnetic resonance (EPR) spectrum analysis was employed utilizing dimethylpyridine nitrogen oxide (DMPO) as a catalyst, as illustrated in Fig. 4a and b. No indications of $^{\bullet}O_2^-$ and $^{\bullet}OH$ were observed without the application of ultrasound vibrations; however, pronounced peak intensities of DMPO $^{\bullet}O_2^-$ and DMPO $^{\bullet}OH$ were observed under ultrasonic vibrations, signifying the tribocatalytic nature of the catalyst. These investigations thus confirmed that both hydroxyl radicals ($^{\bullet}OH$) and superoxide radicals ($^{\bullet}O_2^-$) were generated by optimized (β-FeOOH-100 °C) nanorods throughout the reaction process. The substantial diameter of the optimized (β-FeOOH-100 °C) nanorods, in conjunction with an ultrasonic frequency of 40 kHz, reached its resonance frequency. Consequently, the optimized (β-FeOOH-100 °C) nanorods generated more charges under identical conditions and interacted more vigorously with water molecules than other catalysts. Therefore, in comparison to other catalysts, the optimized β-FeOOH-100 °C catalyst produced a greater quantity of $^{\bullet}OH$ and $^{\bullet}O_2^-$ active radicals as well as a higher tribocurrent density (Fig. 3b).

The respective reaction rate constant k values for these processes of degradation were 0.024, 0.19, and 0.04 min^{-1}, respectively as shown in Fig. 4c. The measured k value for the optimized β-FeOOH-100 °C catalyst was significantly greater than that of other catalysts, indicating the improved tribocatalytic performance of the optimized catalyst. In addition, the stability of the optimized β-FeOOH-100 °C catalyst was further examined by conducting multiple tests on RhB degradation under similar conditions, as illustrated in Fig. 4d. Clearly, there was no decrease in the efficacy of degradation after performing five repeated cycles, which indicates the exceptional stability and ability to be reused of the β-FeOOH-100 °C catalyst. Thus, the result clearly showed that the β-FeOOH-100 °C catalyst exhibited exceptional tribocatalytic activity and excellent stability. Finally, comparative analysis confirms the superior tribocatalytic performance of the β-FeOOH nanorods as shown in Table S1. The tribocatalytic activity of the β-FeOOH-100 material was further assessed through the degradation of RhB under exclusive mechanical stimulation (magnetic stirring in darkness). Remarkably, a 97% degradation efficiency was attained within an 18 hours period (Fig. S7, SI), providing definitive evidence of a tribocatalytically driven process.

To elucidate the roles of various active radicals involved in the process of dye degradation, active species trapping experiments were performed for RhB degradation utilizing BQ, TBA, and EDTA-2Na as scavengers for $^{\bullet}O_2^-$, $^{\bullet}OH$ and h^+, respectively. The UV-vis absorption spectra of the RhB solution as a function of time with various radical scavengers are presented in Fig. 5a and b respectively. Fig. 5a illustrates the impact of the three scavengers on the tribocatalytic efficiency of the optimized catalyst (*i.e.*, β-FeOOH-100) with the resultant k values

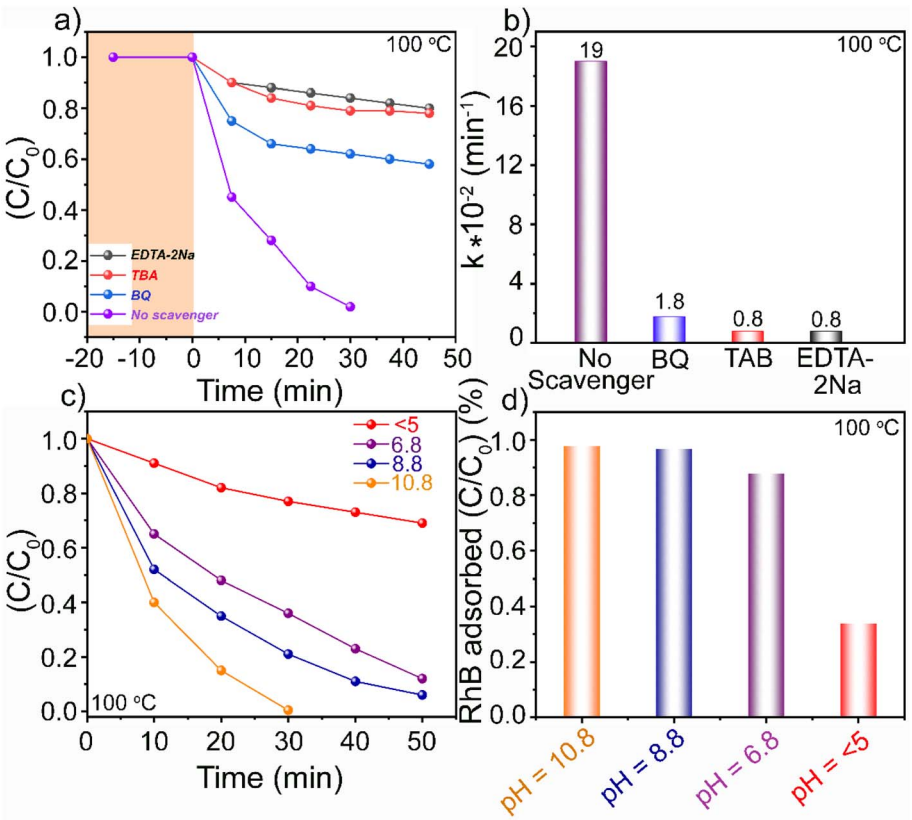

Fig. 5 (a and b) Experiments involving the trapping of active species for RhB degradation, alongside an analysis of the corresponding degradation curve. (c and d) Degradation, and adsorption of RhB dye at various pH values, respectively.

presented in Fig. 5b. The tribocatalytic efficiencies significantly diminished upon the addition of EDTA-2Na (h^+), TBA ($^{\bullet}OH$), and BQ ($^{\bullet}O_2^-$). The results indicated that the friction-induced h^+ and e^- subsequently reacted with H_2O/OH^- and O_2 to generate $^{\bullet}OH$ and $^{\bullet}O_2^-$ active radicals along with h^+, facilitated the degradation of RhB, as seen by the *k* values in Fig. 5b. To further verify the significance of the optimized catalyst we perform the $^{\bullet}OH$ and $^{\bullet}O_2^-$ active radical analysis for all the synthesized catalyst as represented in Fig. S8. It was found that the optimized catalyst generated a greater quantity of both $^{\bullet}OH$ and $^{\bullet}O_2^-$ active radicals than the β-FeOOH-80 and β-FeOOH-120 catalysts, a result that is directly consistent with its superior tribocatalytic performance.

The pH of the reaction medium emerges as a pivotal and governing factor in the tribocatalytic degradation process, critically controlling the interfacial dynamics between the catalyst and the pollutant to dictate overall efficiency. The exceptionally high degradation efficiency of 97% at pH 10.8 is achieved through a synergistic mechanism where the initial adsorption step dictates the overall success of the subsequent catalytic processes as shown in Fig. 5c and d. At this optimal basic pH, the surface of the β-FeOOH nanorods is negatively charged, fostering a powerful electrostatic attraction with the cationic rhodamine B (RhB) dye molecules, which leads to their pronounced pre-concentration onto the catalyst surface. When 40 kHz ultrasound is applied, the resulting acoustic cavitation and violent collapse of microbubbles propel the nanorods into high-velocity collisions, generating intense triboelectric effects that mechanically excite electron–hole pairs (e^-/h^+) on their surfaces. These charge carriers then react to produce a suite of potent reactive oxygen species (ROS), primarily hydroxyl radicals ($^{\bullet}OH$) and superoxide radicals ($^{\bullet}O_2^-$), directly at the solid–liquid interface. Crucially, because the RhB molecules are pre-adsorbed due to the favorable pH, they are positioned perfectly for an immediate and efficient oxidative attack by these ROS, leading to the rapid breakdown of the chromophore, fragmentation of the aromatic structure, and ultimate mineralization into CO_2, H_2O, and simple ions. Thus, the superior performance at pH 10.8 is a direct result of the perfect synergy between maximized dye adsorption and the highly localized, ultrasonic-driven tribocatalytic generation of oxidants, whereas at lower pH values, electrostatic repulsion prevents this crucial interface, leading to significantly lower efficiency.

Based on experimental results, the tribocatalytic reaction mechanism involved in RhB dye degradation is depicted in Fig. S9. The solution continuously rubs the β-FeOOH nanorods and water molecules under ultrasonic vibration. Due to frictional energy, these nanorods accept electrons, while the water molecules lose electrons. This effect persists, effectively maintaining a population of separated charges. Subsequently, the positive holes (h^+) accumulated at the solid–liquid interface facilitate the direct oxidation of organic contaminants, leading to their efficient degradation. At the same time, electrons on the surface of β-FeOOH nanorods connected with O_2 dissolved in the reaction medium, creating $^{\bullet}O_2^-$ radicals. $^{\bullet}O_2^-$ radicals directly degraded the RhB dye, as also confirmed by active species trapping analysis. Moreover, reactive species trapping observations suggested that $^{\bullet}OH$ radicals were crucial in the degradation of RhB as depicted in Fig. 5a. To figure out the cause of $^{\bullet}OH$ radicals, the following main processes were assessed: (1) the gradual reduction of O_2 by electron transfer and (2) the oxidation process involving h^+ and H_2O/OH^-. Regarding the former process, electrons initially interact with O_2 to produce $^{\bullet}O_2^-$ active radical which then converted into H_2O_2, and $^{\bullet}OH$ active radicals. Iodimetry monitoring of H_2O_2 production during the tribocatalytic reaction validated this two-step reductive procedure for $^{\bullet}OH$ production. The progressive increase in H_2O_2 along with quantitative analysis verifies this assumption as shown in Fig. S10.

Conclusions

In conclusion, this study highlights the outstanding tribocatalytic efficiency of the β-FeOOH-100 catalyst in degrading RhB dye under vibrational mechanical stimulation. The catalytic activity was found to be strongly dependent on the nanorod diameter, with larger β-FeOOH nanorods exhibiting superior tribocatalytic behavior. The optimized β-FeOOH-100 sample achieved rapid degradation of RhB, displaying reaction rate constants of 0.024, 0.19, and 0.04 min^{-1}. Moreover, the catalyst maintained excellent stability and reusability over repeated cycles. Mechanistic analysis indicated that friction-induced holes (h^+), together with hydroxyl ($^{\bullet}OH$) and superoxide ($^{\bullet}O_2^-$) radicals, were the dominant reactive species responsible for pollutant decomposition. Considering its simple synthesis route, environmental friendliness, and cost efficiency, the β-FeOOH-100 catalyst demonstrates great potential for practical wastewater treatment applications.

Author contributions

Muhammad Qasim: conceptualization, methodology, writing, original draft, investigation, data analysis, visualization, and supervision. Arslan A. Rizvi: literature review, methodology, writing, review and editing, data analysis, and investigation. Haroon Rashid: methodology, data collection, analysis, and writing, review and editing. Xianglin Li: data curation, investigation, writing, review and editing. Raed H. Althomali: conceptualization, investigation, writing, review and editing, project administration. Hassan A. H. Alzahrani: Hassan A. H. Alzahrani, data analysis, review and editing. Majed M. Alghamdi: data analysis, methodology, and writing, review and editing. Adel A. El-Zahhar: supervision, resources, and project administration, funding acquisition. Sana Ullah Asif: writing review and editing, resources, and project administration. Gideon F. B. Solre: visualization, methodology, and writing, review and editing.

Conflicts of interest

The authors declare that they have no known competing financial interests or personal relationships that could have appeared to influence the work reported in this paper.

Data availability

All the related data is included within the article and available from the authors upon reasonable request.

Supplementary information (SI) is available. See DOI: https://doi.org/10.1039/d5ra06827d.

Acknowledgements

The authors extend their appreciation to the Deanship of Research and Graduate Studies at King Khalid University for funding this work through Large Research Project under grant number RGP2/93/46.

References

1 Z. Xiong, Z. Yi, M. Sakil, L. Huang, Z. Wang, X. Wu, Q. Wang, Z. Wang, G. Zhang, W. Zhang, S. Zhao and L. Zhu, Renewable β-FeOOH nanorods modified polyvinylidene fluoride membrane enables high potable water quality: Performance and mechanisms, *Sep. Purif. Technol.*, 2025, **356**, 129816, DOI: 10.1016/j.seppur.2024.129816.

2 M. Qasim, F. Xue, M. Liu and L. Guo, Phase-transition-induced one-dimensional amorphous α-Fe_2O_3/β-FeOOH homojunction for efficient photocatalytic water oxidation, *J Photonics Energy*, 2019, **9**, 026501, DOI: 10.1117/1.jpe.9.026501.

3 H. Dhila, A. Bhapkar and S. Bhame, Metal oxide/biochar hybrid nanocomposites for adsorption and photocatalytic degradation of textile dye effluents: A review, *Desalin. Water Treat.*, 2025, **321**, 101004, DOI: 10.1016/j.dwt.2025.101004.

4 M. Zhu, Q. Fan, Y. Zhang, S. Chen, W. Cao, R. Xiong, C. Huang, H. Lu and W. Ma, A novel multifunctional photocatalytic membrane based on β-FeOOH for oily wastewater purification, *J. Environ. Chem. Eng.*, 2024, **12**, 114522, DOI: 10.1016/j.jece.2024.114522.

5 Y. Zhang, J. Cui, H. Sun, A. Xie, C. Li, C. Xue and J. Pan, Superwetting polypropylene fiber membrane modified with Co-doped β-FeOOH nanorods for enhanced oil/water separation and self-cleaning, *Mater. Today Chem.*, 2024, **38**, 102050, DOI: 10.1016/j.mtchem.2024.102050.

6 M. Qasim, M. A. Ghanem, X. Cao and X. Li, Modification of α-Fe_2O_3 Nanoparticles with Carbon Layer for Robust Photo-Fenton Catalytic Degradation of Methyl Orange, *Catalysts*, 2024, **14**, 393, DOI: 10.3390/catal14060393.

7 J. Luo, X. Liu, J. Gu, W. Zhao, M. Gu and Y. Xie, Construction of novel g-C_3N_4/β-FeOOH Z-Scheme heterostructure photocatalyst modified with carbon quantum dots for efficient degradation of RhB, *J. Mater. Sci. Technol.*, 2024, **181**, 11–19, DOI: 10.1016/j.jmst.2023.10.006.

8 C. Han, C. Xie, R. Wang, C. Deng and P. Zhao, Glucose assisted synthesis of the BiOCl/β-FeOOH composite with enhanced photocatalytic performance, *Mater. Lett.*, 2016, **181**, 16–20, DOI: 10.1016/j.matlet.2016.05.134.

9 W. Ma, Y. Zhang, Y. Li, Y. Wang, R. Sun, Y. Wu and C. Han, The formation of uniform straw-like β-FeOOH nanostructures with superior catalytic performance for the degradation of Rhodamine B, *J. Nanopart. Res.*, 2021, **23**, 19, DOI: 10.1007/s11051-020-05116-x.

10 L. Liu, W.-T. Chen, S. Kihara and P. A. Kilmartin, Green synthesis of akaganéite (β-FeOOH) nanocomposites as peroxidase-mimics and application for discoloration of methylene blue, *J. Environ. Manage.*, 2021, **296**, 113163, DOI: 10.1016/j.jenvman.2021.113163.

11 K. Xie, J. Fang, L. Li, J. Deng and F. Chen, Progress of graphite carbon nitride with different dimensions in the photocatalytic degradation of dyes: A review, *J. Alloys Compd.*, 2022, **901**, 163589, DOI: 10.1016/j.jallcom.2021.163589.

12 N. Sreedhar, M. Kumar, S. Al Jitan, N. Thomas, G. Palmisano and H. A. Arafat, 3D printed photocatalytic feed spacers functionalized with β-FeOOH nanorods inducing pollutant degradation and membrane cleaning capabilities in water treatment, *Appl. Catal., B*, 2022, **300**, 120318, DOI: 10.1016/j.apcatb.2021.120318.

13 A. A. Abbas, G. Jingsong, L. Z. Ping, P. Y. Ya and W. S. Al-Rekabi, Review on landfill leachate treatments, *Am. J. Appl. Sci.*, 2009, **6**, 672–684, DOI: 10.3844/ajas.2009.672.684.

14 I. Anastopoulos, M. J. Ahmed, V. E. Ojukwu, M. Danish, M. Stylianou and J. O. Ighalo, A comprehensive review on adsorption of Reactive Red 120 dye using various adsorbents, *J. Mol. Liq.*, 2024, **394**, 123719, DOI: 10.1016/j.molliq.2023.123719.

15 M. Qasim, A. M. Iqbal, M. T. Khan and M. A. Ghanem, Nanostructural Modification of Fe_2O_3 Nanoparticles: Carbon Coating for Enhanced Magnetic Behavior, *Phys. Status Solidi RRL*, 2025, **19**, 2400230, DOI: 10.1002/pssr.202400230.

16 M. Qasim, M. Liu and L. Guo, Electron transfer *via* a carbon channel for efficient Z-scheme solar hydrogen production, *Int. J. Hydrogen Energy*, 2021, **46**, 28098–28109, DOI: 10.1016/j.ijhydene.2021.06.074.

17 M. Gao, L. Sun, C. Ma, X. Li, H. Jiang, D. Shen, H. Wang and P. Huo, Constructed Z-Scheme g-C_3N_4/Ag_3VO_4/rGO Photocatalysts with Multi-interfacial Electron-Transfer Paths for High Photoreduction of CO_2, *Inorg. Chem.*, 2021, **60**, 1755–1766, DOI: 10.1021/acs.inorgchem.0c03233.

18 M. Qasim, M. Liu and L. Guo, Z-scheme P-doped-g-C_3N_4/Fe_2P/red-P ternary composite enables efficient two-electron photocatalytic pure water splitting, *Catal. Today*, 2023, **409**, 119–127, DOI: 10.1016/j.cattod.2022.05.007.

19 X. Zhang, K. Matras-Postolek, P. Yang and S. Ping Jiang, Z-scheme WOx/Cu-g-C_3N_4 heterojunction nanoarchitectonics with promoted charge separation and transfer towards efficient full solar-spectrum photocatalysis, *J. Colloid Interface Sci.*, 2023, **636**, 646–656, DOI: 10.1016/j.jcis.2023.01.052.

20 A. Gaur, N. Saurabh and S. Patel, Pyrocatalysis-driven dye degradation by Zn Doped NBT-BT: A comparative analysis between powder and bulk, *Mater. Chem. Phys.*, 2024, **315**, 128940, DOI: 10.1016/j.matchemphys.2024.128940.

21 Y. Guo, T. Li, D. Li and J. Cheng, Efficient reduction of CO_2 to high value-added compounds *via* photo-thermal catalysis: Mechanisms, catalysts and apparatuses, *Renewable*

Sustainable Energy Rev., 2024, **189**, 114053, DOI: 10.1016/j.rser.2023.114053.

22 H. Zheng, Y. Wang, J. Liu, J. wang, K. Yan and K. Zhu, Recent advancements in the use of novel piezoelectric materials for piezocatalytic and piezo-photocatalytic applications, *Appl. Catal., B*, 2024, **341**, 123335, DOI: 10.1016/j.apcatb.2023.123335.

23 S. Tu, Y. Guo, Y. Zhang, C. Hu, T. Zhang, T. Ma and H. Huang, Piezocatalysis and Piezo-Photocatalysis: Catalysts Classification and Modification Strategy, Reaction Mechanism, and Practical Application, *Adv. Funct. Mater.*, 2020, **30**, 2005158, DOI: 10.1002/adfm.202005158.

24 Q. Zhang, Y. Jia, X. Wang, L. Zhang, G. Yuan and Z. Wu, Efficient tribocatalysis of magnetically recyclable cobalt ferrite nanoparticles through harvesting friction energy, *Sep. Purif. Technol.*, 2023, **307**, 122846, DOI: 10.1016/j.seppur.2022.122846.

25 A. Shukla, A. Gaur, V. S. Chauhan and R. Vaish, Sonocatalysis and tribocatalysis for dye degradation using $Ca_2Fe_2O_5$, *J. Mater. Res.*, 2025, **40**, 803–818, DOI: 10.1557/s43578-025-01536-4.

26 X. Li, W. Tong, J. Shi, Y. Chen, Y. Zhang and Q. An, Tribocatalysis mechanisms: electron transfer and transition, *J. Mater. Chem. A*, 2023, **11**, 4458–4472, DOI: 10.1039/d2ta08105a.

27 M. Wu, Y. Zhang, Y. Yi, B. Zhou, P. Sun and X. Dong, Regulation of friction pair to promote conversion of mechanical energy to chemical energy on Bi_2WO_6 and realization of enhanced tribocatalytic activity to degrade different pollutants, *J. Hazard. Mater.*, 2023, **459**, 132147, DOI: 10.1016/j.jhazmat.2023.132147.

28 Y. Wang, S. Shen, M. Liu, G. He and X. Li, Enhanced tribocatalytic degradation performance of organic pollutants by $Cu_{1.8}S/CuCo_2S_4$ p–n junction, *J. Colloid Interface Sci.*, 2024, **655**, 187–198, DOI: 10.1016/j.jcis.2023.10.164.

29 S. Sun, X. Sui, H. Yu, Y. Zheng, X. Zhu, X. Wu, Y. Li, Q. Lin, Y. Zhang, W. Ye and Y. Liang, High Tribocatalytic Performance of FeOOH Nanorods for Degrading Organic Dyes and Antibiotics, *Small Methods*, 2024, **8**(12), 2301784, DOI: 10.1002/smtd.202301784.

30 M. Qasim, F. Xue, M. Liu and L. Guo, Phase-transition-induced one-dimensional amorphous α-Fe_2O_3/β-FeOOH homojunction for efficient photocatalytic water oxidation, *J Photonics Energy*, 2019, **9**(2), 026501, DOI: 10.1117/1.jpe.9.026501.

31 J. Fan, Z. Zhao, Z. Ding and J. Liu, Synthesis of different crystallographic FeOOH catalysts for peroxymonosulfate activation towards organic matter degradation, *RSC Adv.*, 2018, **8**, 7269–7279, DOI: 10.1039/C7RA12615H.

32 Q. Zhuang, X. Li, X. Lian, H. Hu, N. Wang, J. Wu, K. Miao, G. Feng and X. Luo, Catalysis Enhancement of Co_3O_4 through the Epitaxial Growth of Inert ZnO in Peroxymonosulfate Activation: The Catalytic Mechanism of Surface Hydroxyls in Singlet Oxygen Generation, *Cryst. Growth Des.*, 2025, **25**, 319–329, DOI: 10.1021/acs.cgd.4c01357.

33 D. S. Chaudhari, R. P. Upadhyay, G. Y. Shinde, M. B. Gawande, J. Filip, R. S. Varma and R. Zbořil, A review on sustainable iron oxide nanoparticles: syntheses and applications in organic catalysis and environmental remediation, *Green Chem.*, 2024, **26**, 7579–7655, DOI: 10.1039/D4GC01870B.

34 M. Guo, Z. Jin, J. Pan, J. Xu, L. Guo, X.-B. Yin, N. Lu and M. Zhang, Construction of COFs@MoS_2-Pd Hierarchical Tubular Heterostructures for Enhanced Catalytic Performance, *Inorg. Chem.*, 2024, **63**, 18263–18275, DOI: 10.1021/acs.inorgchem.4c03151.